Interior heating drives the formation of clouds on exoplanet gas giants

Orkun Temel[1], Hakan Sert[1], Cem Berk Senel[1], Tim Van Hoolst[1], and Özgür Karatekin[1]

[1]Royal Observatory of Belgium

November 21, 2022

Abstract

We investigate the formation of water ice, ammonia ice and ammonia hydrosulphide clouds on exoplanet gas giants for various internal heat fluxes using the modified version of the PlanetWRF model, GasGiantWRF. We performed our model calculations using a newtonian thermal forcing, described by an analytical radiative model, and a cloud scheme that allows the phase exchange between different species relevant to a Jupiter-like exoplanet. We show strong variations in the concentration of water ice and ammonia ice clouds, up to four and two orders of magnitudes respectively with varying interior heat fluxes, between 1.35 and 10.8 W/m2 for a Jupiter-like exoplanet.

Interior heating drives the formation of clouds on exoplanet gas giants

Orkun Temel[1,2], Hakan Sert[2], Cem Berk Senel[2], Tim Van Hoolst[2,1] and Özgür Karatekin[2]

[1]KU Leuven, Institute of Astronomy, Leuven, Belgium
[2]Royal Observatory of Belgium, Brussels, Belgium

Key Points:

- We applied the PlanetWRF model to gas giants.
- We investigated the effect of interior heating on clouds in Jupiter-like exoplanets.
- We find a strong variation of cloud abundance with interior heating, up to 4 orders of magnitude in mixing ratio.

Corresponding author: Orkun Temel, `orkun.temel@oma.be`

Abstract

We investigate the formation of water ice, ammonia ice and ammonia hydrosulphide clouds on exoplanet gas giants for various internal heat fluxes using the modified version of the PlanetWRF model, GasGiantWRF. We performed our model calculations using a newtonian thermal forcing, described by an analytical radiative model, and a cloud scheme that allows the phase exchange between different species relevant to a Jupiter-like exoplanet. We show strong variations in the concentration of water ice and ammonia ice clouds, up to four and two orders of magnitudes respectively with varying interior heat fluxes, between 1.35 and 10.8 W/m^2 for a Jupiter-like exoplanet.

Plain Language Summary

Following the discovery of the first exoplanet, many extrasolar gas giants, similar to Jupiter in our solar system in terms of their size and mass, have been discovered. Jupiter's atmosphere harbors clouds, composed of ammonium and water. The formation of these clouds is driven by the thermal structure of Jupiter. For Earth, the primary source of heat is the solar radiative heating. Whereas, the interior heating of the planet plays a crucial role on the weather patterns of Jupiter. In this study, we performed numerical weather forecasting simulations to understand the effect of interior heating on the formation of clouds on extrasolar planets similar to Jupiter, We have found that the abundance of clouds can vary up to four (for water ice clouds) and two (for ammonia ice clouds) with varying interior heating.

1 Introduction

Photometric and spectroscopic surveys show a high occurrence of Jupiter-analog exoplanets, up to 6.74% according to the Anglo-Australian Planet Search database (Wittenmyer et al., 2016). For the case of star systems hosting a Super-Earth, the occurrence rate is estimated to be up to 39% (Bryan et al., 2019). Properties of the atmospheres can be obtained from observations of the stellar light passing through the atmosphere (Dalba et al., 2015). Transmission spectra can for example be used to predict the mixing ratios of tracers in the atmosphere, given a thermal profile (Fortney et al., 2010). Obtaining atmospheric mixing ratios can be strenuous in the presence of clouds or haze (Knutson et al., 2014). Therefore, it is important to understand under which conditions, the atmospheres of exoplanet gas giants can be cloudier. This can be achieved by performing atmospheric model simulations. Moroever, recent observations used the direct imaging techniques for exoplanet gas giants, which makes use of the variation of cloud mixing ratios and cloud effective particle radius as an input (Marley & Sengupta, 2011). In addition to the possible implications of modeling the clouds in exoplanet gas giants, Jovian and planetary-mass brown dwarf atmospheres have been studied in terms of assessing their atmospheric habitability zones using atmospheric models, which are capable of predicting of aerosol distributions (or aeroplankton) (Sagan & Salpeter, 1976; Yates et al., 2017). The transport of aerosols, whether cloud particles or bio-aerosols, is driven by three main processes: 1) uplifting of particles with vertical wind, 2) sedimentation of particles to the lower part of the atmosphere due to gravitational force, and 3) the horizontal transport with the global circulation. All these processes are affected by the thermal structure of the atmosphere: The magnitude of vertical winds is related to the temperature gradient of atmosphere; the gravitational settling of particles is driven by the terminal sedimentation velocity, which is calculated as a function of atmospheric temperature and pressure (Lee et al., 2010); and thermal forcing is one of the main parameters driving the global circulation in addition to orbital forcing. Hence, it is important to understand how the cloud formation of exoplanet gas giants change with the thermal structure of the atmosphere.

Our current understanding of the atmospheric dynamics and cloud formation of gas giants is mostly based on the observations of the Jovian and Saturnian atmospheres with the past and ongoing missions: Pioneer (Kliore et al., 1974) and Vogayer (Eshleman et al., 1979) programmes, Galileo probe and orbiter (Niemann et al., 1996; Seiff et al., 1996), Ulysses (Lanzerotti et al., 1992), Cassini (Porco et al., 2003), and the ongoing Juno orbiter mission (Bolton et al., 2017). The Galileo probe observed the atmosphere down to 12 bars and showed the presence of clouds between 0.46 and 4.5 bars (Ragent et al., 1998). The clouds of Jupiter is mainly composed of ammonia gas/ice, water vapor/ice and ammonium hydrosulphide crystals. And, later Juno orbiter performed observations on the distribution of ammonia (C. Li et al., 2017). It was reported that the ammonia ice crystals can not be formed at depths, where the atmospheric pressure is higher than 1 bar despite the high amount of ammonia gas that can reach down to 60 bars (Bolton et al., 2017). The exact altitude range of cloud layer depends on the production and destruction of mechanisms of aerosols, such as uplifting by vertical winds, sedimentation and phase change. These processes will be investigated by the JUICE mission (Grasset et al., 2013). Nevertheless, the observational findings with the past and current missions to Jupiter constrain the pressure range of clouds, showing that atmospheric models, that focuses on the cloud layer of Jupiter from a dynamic and microphysical perspective, should cover the deep troposphere, which corresponds to several bars (Grassi et al., 2017).

Earth based observations (Smoluchowski, 1967) show that Jupiter radiates significantly more energy than it absorbs from the Sun. Jupiter's radiant energy budget is recently re-evaluated from the analyses of Cassini multi-instrument observations data sets (L. Li et al., 2018). The ratio of the emitted thermal power over the absorbed solar power is more than a factor 2 and the determined internal heat value $7.485W/m^2$ is significantly larger than the previous results ($5.444W/m^2$) from the Infrared observations of Pioneer and Voyager. The effective temperatures of cold Jupiter-like would also likely exceed the predicted equilibrium temperature. The interior heat flux will change the vertical structure of the atmosphere. As formulated by an analytical radiative model of (Robinson & Catling, 2012), the stronger the internal heat flux is, the higher the temperature gradient will be. This will not only affect the atmospheric mixing, driving the transport of clouds, but also lead to different vertical variations of temperature, which will change the sedimentation rate of cloud particles (Lee et al., 2010) and thus affect the formation of clouds. Modeling work on Jupiter and Jupiter-like gas giants mostly focused on the formation of jets and its relation to moist transport processes (Lian & Showman, 2008; Kaspi et al., 2009; Lian & Showman, 2010, 2009; O'Neill et al., 2015; Young et al., 2019b). The effect of internal heat on deep convection and jet streams have been discussed previously but its affect the on the clouds have not been addressed (Ingersoll et al., 2004). Here, we focus on the effect of interior heating on the formation of clouds on Jupiter-like exoplanets. Because of belts and zones on Jupiter and Saturn, modeling the cloud formation on Jupiter-like exoplanets requires three dimensional atmospheric modeling capable of predicting cloud formation process (with a microphysics scheme which considers the phase exchange between the transported species). Here, we perform three-dimensional atmospheric model simulations to understand the variation of clouds over a range of interior heat fluxes for a Jupiter-like exoplanet.

The paper is organized as follows: In Section 2, we present a brief description of our global circulation model (GCM) that we adapted from the PlanetWRF model, in Section 3, we present our results and describe the formation of water ice, ammonia ice and ammonia hydrosulphide clouds. And finally we present our conclusions in Section 4.

2 Model description

In this study, we use the PlanetWRF model, a three-dimension global circulation model (Richardson et al., 2007) based on the terrestrial Weather Research and Forecasting (WRF) model (Skamarock et al., 2008). Despite that it was successfully applied to Mars (Senel et al., 2021; Temel et al., 2021), Titan (Newman et al., 2011, 2016) and Pluto (Toigo et al., 2015), it does not include a variant for gas giant atmospheres. Here we use its dynamical core to adapt our GCM to Jupiter-like exoplanets and develop the gas giant variant of PlanetWRF (hereafter GasGiantWRF). To do so, we first implement a radiative forcing, that can produce both the vertical and horizontal thermal structure of a Jupiter-like exoplanet in a simple and efficient way. The second step is to implement a cloud scheme, which calculates the phase exchange between species relevant to a Jupiter-like exoplanet.

For thermal forcing, we have chosen to use a simple Newtonian forcing scheme, which allows us to perform simulations in a relatively shorter spin-up time compared to sophisticated radiative models applicable to the atmosphere of Saturn and Jupiter (Guerlet et al., 2014; Young et al., 2019b, 2019a). To compute the vertical variation of temperature, we use an analytical radiative model applicable for Jupiter that takes the internal heat flux into account (Robinson & Catling, 2012). This model is based on solving the two-stream radiative flux equation with a boundary condition that includes the balance of solar fluxes in two shortwave channels at the top of the atmosphere, F_1 and F_2, and the interior heat flux, F_i. By using two separate solar fluxes, instead of a single one, the model is able to produce the distinct tropospheric and stratopspheric thermal structures. The chosen analytical model had already been applied to the atmosphere of Jupiter with a reasonable agreement by (Robinson & Catling, 2012; Tolento & Robinson, 2019). The analytical solution of the radiative flux equation which we use to force our model follows:

$$\sigma T^4(\tau) = \frac{F_1}{2}\left[1 + \frac{D}{k_1} + \left(\frac{k_1}{D} - \frac{D}{k_1}\right)e^{-k_1\tau}\right] + \frac{F_2}{2}\left[1 + \frac{D}{k_2} + \left(\frac{k_2}{D} - \frac{D}{k_2}\right)e^{-k_2\tau}\right] + \frac{F_i}{2}(1 + D\tau) \tag{1}$$

We set the parameters in Eq. 1 similar to the Jupiter setup of (Robinson & Catling, 2012). Here, D is the diffusivity factor taken as 1.88, σ is the Stefan-Boltzmann constant (5.67 x 10^{-8} W/m^{-2}K^{-4}). F_1 and F_2 are the top-of-the atmosphere stellar fluxes in two shortwave channels, set as 7.0 and 1.3 W/m^{-2} and parameterized by the attenuation coefficients k_1 and k_2, which are 100 and 0.06 respectively. F_i is the internal heat flux and τ is the optical thickness of the atmosphere. Here, we investigate a range of internal heat flux between 1.35 W/m^{-2} and 10.8 W/m^{-2}, which covers the estimated internal heat fluxes for Saturn (2.01 W/m^{-2} (Hanel et al., 1983)) and Jupiter (previously estimated to be around 5.4 W/m^{-2} from Voyager Infrared investigations (Hanel et al., 1981) and recently updated to 7.4 W/m^{-2} based on from Cassini CIRS and VIMS observations (L. Li et al., 2018)). The optical depth is calculated as a function of atmospheric pressure:

$$\tau = \tau_0 \left(\frac{p}{p_0}\right)^n \tag{2}$$

In Eq. 2, τ_0 is a reference optical depth, which is set to 3.15, p_0 is the reference pressure for the analytical model, set to 1.0 bar. The proportionality coefficient parameterizes the dependency of optical depth on pressure. It does not have a universal value but typically, it varies between 1 and 2 (Heng et al., 2012). In case of weak-dependency of optical depth on pressure, when the absorbing gas is well mixed, it is taken as 1 (Robinson & Catling, 2012). When the concentration of the absorbing gas has a strong variation with pressure, it can be set to larger values than 2, as in the case of modeling Earth's troposphere (Frierson et al., 2006). Here, we set it to 1.5. The resulting forcing scenarios in comparison with (Moses et al., 2005) dataset is given in Fig. 1.

We run our model with 144 x 72 resolution on zonal and meridional direction and consists of 36 vertical levels from 20 bars to 0.01 bars to cover the stratosphere and troposphere of a Jupiter-like exoplanet. The altitude range covered by our model is consistent with the pressure ranges where the clouds are expected to form on Jupiter. With a deeper bottom boundary, the model can also cover the formation of deep jets (Lian & Showman, 2008), but the formation of those very deep jets do not affect the formation of jets at 1 bar, where we expect the formation of clouds (see Fig. 5 of (Lian & Showman, 2008)). We perform our model simulations for planetary parameters (i.e planetary radius, rotation period) for Jupiter but without any seasonal variation. In other words, we do not change the imposed thermal forcing profile for a given eccentricity or obliquity and assume that both are zero.

The temperature profiles given in Fig. 1, represent the globally averaged state of the atmosphere. We include latitudinal variations with a sinusoidal formulation, as suggested by (Lian & Showman, 2008), to produce the hot-and-cold latitude bands that are observed on Jupiter:

$$T_{eq}(\phi, p) = T_{ref}(p) + \delta T \tag{3}$$

In Eq. 4, T_{eq} is the temperature that GasGiantWRF is being forced, T_{ref} is the atmospheric temperature at each model layer, presented in Fig. 1. δT is the latitudinal forcing term, which is applied in a latitudinal range of $\phi = [75°S, 75°N]$, but is zero otherwise.

$$\delta T = 5.0cos^2(8\phi) \tag{4}$$

We do not enforce an equator-to-pole temperature difference in our thermal forcing, consistent with the temperature observations of TEXES, which showed that Jupiter's troposphere does not have a monotonic meridional temperature gradient and it has weak temperature variations up to 2 K (Fletcher et al., 2016).

Our cloud scheme is adapted from Oxford's Jupiter General Circulation Model in terms of cloud formation, sedimentation and initial condensate concentrations. The cloud scheme consists of six tracers: water vapor [H_2O(g)], water ice [H_2O(s)], gaseous ammonia [NH_3(g)], ammonia ice [NH_3(s)], hydrogen sulphide [H_2S(g)], ammonium hydrosulphide [NH_4SH(s)]. All these species are transported as passive tracers, not affecting the thermal forcing. The condensate particles are subject to sedimentation with a single fixed particle radius, which is set to 10 microns. For the water cycle, water ice clouds are formed, where the atmosphere is saturated with water vapor at each model layer. In case of saturation, the excess amount is converted into water ice. When it is transported to an altitude or region where the atmosphere is not saturated, the water ice clouds are converted back to water vapor. We did not include rain droplets based on the assumption that the water droplets will be fully evaporated within a time scale that is smaller than our computational timestep, which is 600 seconds. The same phase change process applies for the ammonia cycle (The reader is referred to (Young et al., 2019a) for details, see Section A.2 in (Young et al., 2019a)). We also include the formation of ammonium hydrosulphide clouds by the reaction of ammonia vapor and hydrogen sulphide when the partial pressures of hydrogen sulphide and gaseous ammonia exceeds a reaction limit as a function of atmospheric temperature, $exp(34.137 - 10834/T)$ (see Section A.4 in (Young et al., 2019a)). The altitude ranges, where water ice, ammonia ice and ammonium hydrosulphide clouds can form based on initial conditions, are presented in Fig. 2.

3 Results

Similar to previous studies on gas-giant atmospheres (Lian & Showman, 2008; Showman et al., 2010; Young et al., 2019b), we first performed a spin-up run, which is needed to ensure that the zonal jets are formed. Following the spin-up period, we investigate the global and vertical variations of winds and tracers of water and ammonia cycles.

Fig. 3 presents the predicted zonal and vertical winds for three internal heat flux forcing cases (hereafter case-L: 1.35 W/m^2, case-M: 5.40 W/m^2, case-H: 10.80 W/m^2). At 0.1 bar (left panel), we observe zonal jets with latitudinal sizes similar to those of the thermal forcing. For the case-L, the circulation at 0.1 bars is associated with a strong zonal and a very weak meridional transport. With increasing interior heat flux, vertical temperature gradients increase, as given in Fig. 1, which lead to higher mixing and enhance meridional transport (see left planel of Fig. 3). For the vertical variation of zonal winds, we find that for each case an equatorial zonal jet forms. The vertical extent of this super-rotating zonal jet goes deeper with increasing interior heating. Despite that the vertical extent of the jet reaches slightly below 1 bar for case-L, the jet extends much deeper for case-M and especially case-H. The higher the internal heat flux is, the higher the temperature gradient is in the lower troposphere between 20 and 1 bars, which leads to a deeper equatorial zonal jet. The effect of the higher temperature gradient is also evident in the variation of vertical wind speeds. With the increasing vertical temperature gradient, the vertical mixing enhances and the vertical wind speeds vary remarkably between different interior heat fluxes as shown in Fig.3, possibly enhancing the vertical transport of tracers.

In Fig. 4 we investigate how the internal heat flux affects the water cycle on an exoplanet gas giant. For case-L, we find that water vapor is distributed within the latitudinal bands, mostly in the equatorial band. With increasing interior heat flux, water vapor aggregates within two main mid-latitude bands, possibly as a result of the increasing meridional transport as depicted in Fig. 3. It must be noted that the column integrated cloud species are not time-averaged but corresponds to the instantaneous state of the atmosphere. Therefore, the discontinuity of the Northern hemisphere water vapor band is not as a result of stationary atmospheric structure. In terms of its vertical variation, for case-L, water vapor tends to be concentrated close to the lower boundary at 20 bars. This is as a result of the low vertical velocity caused by the low temperature gradients. Water vapor is well mixed within troposphere for case-M and case-H, reaching high concentrations up to 1 bar.

Water ice clouds follows a similar pattern to the distribution of water vapor. For case-L, we find that the water ice clouds mainly form on the equatorial belt, where the water vapor concentration is the highest. However, our results also show denser water ice clouds in the zonal direction. As in the case of water vapor bands for case-H, this is due to the fact that we present results for an instantaneous state of the atmosphere. Column integrated water ice concentrations are higher for case-M and H and the latitudinal extend of mid-latitude water ice clouds bands slightly enlarges for case-H, with respect to case-M. In terms of the vertical variation of water ice clouds, we find that the thickness of water ice clouds increase with the interior heating and the clouds start to form at a higher altitude. C15: This is because, with the higher troposphere temperatures, the lower atmosphere can be saturated to a higher level of water vapor as shown in Fig.2. This allows the formation of cloud-deck at a higher altitude with a higher interior heating rate.

In Fig. 5, we focus on the variation of ammonia cycle, which includes the formation of ammonia ice clouds by phase change and ammonia hydrosulphide clouds via chemical reaction. The horizontal transport of ammonia ice and gaseous ammonia shows similarities with the transport of water vapor and water ice. For case-L, the gaseous ammonia and ammonia ice are confined to the equatorial band, which is extended in the latitudinal direction and dispersed to the mid-latitude bands with increasing interior heating (case-M and case-H). However, for hydrogen sulphide, we do not observe the formation of high concentration mid-latitude zones as in the case of ammonia ice and gaseous ammonia. Since it is depleted by the formation of ammonium hydrosulphide clouds which form at the equatorial band and then emerge to the mid latitude bands with higher interior heating. Ammonium hydrosulphide clouds, as a product of gaseous hydrogen sulphide and ammonia tracers, mostly form at the equatorial zonal jet for case-L. For case-M and case-H, these clouds form at a wider latitudinal range. Despite the similarity between the horizontal transport of water vapor, gaseous ammonia is well mixed within troposphere for case-L and case-M. We also find that gaseous ammonia can reach up to the stratosphere unlike the case for water vapor with interior heat flux forcing, case-H. Moreover, On contrary to water ice clouds, our calculations reveal that ammonia ice can form in the upper parts of troposphere even under the lowest interior heat flux forcing.

We finally investigate the variation of globally averaged column integrated water vapor and water ice for nine interior heat flux values in Fig. 6. Our results show that variations in the interior heat flux can result up to almost a four orders of magnitude changes in the column abundance of water ice clouds. We observe a non monotonic variation of water ice cloud content over the range of interior heating fluxes we consider in our present study. For a very low interior heat flux, such as 1.35 W/m^2, the atmosphere is more saturated into water vapor, compared to the cases with interior heat fluxes of 2.0 and 2.7 W/m^2. Thus, an higher amount of excess water vapour is converted into water ice. Therefore, we find that for a Jupiter-like exoplanet with an interior heating of around 2.7 W/m^2 can be one order of magnitude less cloudy than 1.35 W/m^2. With the increasing interior heat flux, and temperature, the atmosphere can hold more water vapor. However, we observe that the atmosphere contains higher amounts of water ice for interior heat fluxes, larger than 2.7 W/m^2. Despite that the atmosphere is even less saturated so that a higher amount of water vapor can be held at each atmospheric layer, as presented in Fig. 4, water vapor can be transported to upper layers of atmosphere, thanks to the higher vertical velocity. This allows the formation of water ice clouds at a higher altitude with a higher interior heating. As a result of lower pressure at the altitude ranges, where the water ice clouds can form, they also form under a higher mixing ratio, causing three orders of magnitude of variations in the globally averaged water ice concentrations. We find that after 5.4 W/m^2, this enhancement of water ice mixing ratio reaches to an equilibrium. Similar to the water cycle, we also find that two orders of magnitude variation occurs with varying interior heat fluxes for ammonia ice clouds. A lower variation exists for ammonia hydrosulphide clouds.

4 Conclusions

We investigated the relationship of various tracers, related to ammonia and water cycles, on a Jupiter-like exoplanet for various interior heat fluxes. We found that with increasing interior heat flux, vertical transport in the atmosphere enhances and leads the water vapor and gaseous ammonia to be transported well above the deep troposphere, affecting the altitude of ammonia ice, water ice and ammonium hydrosulphide clouds. We also report that for low interior heat fluxes, tracers are aggregated within a narrow latitude band, corresponding to the equatorial zonal jet. With increasing interior heat flux, clouds from two mid-latitude bands. Moreover, our results revealed that the concentration of cloud condensates can change up to orders or magnitudes with varying interior heat fluxes, showing that interior heating is one of the main drivers of cloud formation mechanism on exoplanet gas giants. We performed our calculations using a single particle size, in a subsequent study, we will conduct model simulations capable of transporting cloud aerosols with varying particle radius and investigate how the particle radius of aerosols change with different interior heat forcing. Moreover, the simplicity of our thermal forcing prevents our gas giant model to be applied as an operational atmospheric model to Jupiter's atmosphere. In a subsequent study, we are planning to implement a more realistic radiative parameterization, perform higher-resolution GCM simulations and compare our predictions with the observations.

Acknowledgments
This work was financially supported by grant 12ZZL20N (to Orkun Temel) of the Research Foundation Flanders (FWO). Ozgur Karatekin and Tim Van Hoolst acknowledge the support of BELSPO through the ESA/PRODEX Program. Cem Berk Senel was supported by the Belgian Science Policy Office (BELSPO) via Chicxulub BRAIN-be (Belgian Research Action through Interdisciplinary Networks) project. The data presented in the manuscript is available online (https://doi.org/10.17605/OSF.IO/9SPW3).

References

Bolton, S. J., Adriani, A., Adumitroaie, V., Allison, M., Anderson, J., Atreya, S., . . . others

(2017). Jupiter's interior and deep atmosphere: The initial pole-to-pole passes with the juno spacecraft. *Science*, *356*(6340), 821–825.

Bryan, M. L., Knutson, H. A., Lee, E. J., Fulton, B., Batygin, K., Ngo, H., & Meshkat, T. (2019). An excess of jupiter analogs in super-earth systems. *The Astronomical Journal*, *157*(2), 52.

Dalba, P. A., Muirhead, P. S., Fortney, J. J., Hedman, M. M., Nicholson, P. D., & Veyette, M. J. (2015). The transit transmission spectrum of a cold gas giant planet. *The Astrophysical Journal*, *814*(2), 154.

Eshleman, V., Tyler, G., Wood, G., Lindal, G., Anderson, J., Levy, G., & Croft, T. (1979). Radio science with voyager 1 at jupiter: Preliminary profiles of the atmosphere and ionosphere. *Science*, *204*(4396), 976–978.

Fletcher, L. N., Greathouse, T., Orton, G., Sinclair, J., Giles, R., Irwin, P., & Encrenaz, T. (2016). Mid-infrared mapping of jupiter's temperatures, aerosol opacity and chemical distributions with irtf/texes. *Icarus*, *278*, 128–161.

Fortney, J., Shabram, M., Showman, A., Lian, Y., Freedman, R., Marley, M., & Lewis, N. (2010). Transmission spectra of three-dimensional hot jupiter model atmospheres. *The Astrophysical Journal*, *709*(2), 1396.

Frierson, D. M., Held, I. M., & Zurita-Gotor, P. (2006). A gray-radiation aquaplanet moist gcm. part i: Static stability and eddy scale. *Journal of the atmospheric sciences*, *63*(10), 2548–2566.

Grasset, O., Dougherty, M., Coustenis, A., Bunce, E., Erd, C., Titov, D., ... others (2013). Jupiter icy moons explorer (juice): An esa mission to orbit ganymede and to characterise the jupiter system. *Planetary and Space Science*, *78*, 1–21.

Grassi, D., Adriani, A., Mura, A., Dinelli, B., Sindoni, G., Turrini, D., ... others (2017). Preliminary results on the composition of jupiter's troposphere in hot spot regions from the jiram/juno instrument. *Geophysical Research Letters*, *44*(10), 4615–4624.

Guerlet, S., Spiga, A., Sylvestre, M., Indurain, M., Fouchet, T., Leconte, J., ... others (2014). Global climate modeling of saturn's atmosphere. part i: Evaluation of the radiative transfer model. *Icarus*, *238*, 110–124.

Hanel, R., Conrath, B., Herath, L., Kunde, V., & Pirraglia, J. (1981). Albedo, internal heat, and energy balance of jupiter: Preliminary results of the voyager infrared investigation. *Journal of Geophysical Research: Space Physics*, *86*(A10), 8705–8712.

Hanel, R., Conrath, B., Kunde, V., Pearl, J., & Pirraglia, J. (1983). Albedo, internal heat flux, and energy balance of saturn. *Icarus*, *53*(2), 262–285.

Heng, K., Hayek, W., Pont, F., & Sing, D. K. (2012). On the effects of clouds and hazes in the atmospheres of hot jupiters: semi-analytical temperature–pressure profiles. *Monthly Notices of the Royal Astronomical Society*, *420*(1), 20–36.

Ingersoll, A. P., Dowling, T. E., Gierasch, P. J., Orton, G. S., Read, P. L., Sánchez-Lavega, A., ... Vasavada, A. R. (2004). Dynamics of jupiter's atmosphere. *Jupiter: The planet, satellites and magnetosphere*, *105*.

Kaspi, Y., Flierl, G. R., & Showman, A. P. (2009). The deep wind structure of the giant planets: Results from an anelastic general circulation model. *Icarus*, *202*(2), 525–542.

Kliore, A., Cain, D. L., Fjeldbo, G., Seidel, B. L., & Rasool, S. (1974). Preliminary results on the atmospheres of io and jupiter from the pioneer 10 s-band occultation experiment. *Science*, *183*(4122), 323–324.

Knutson, H. A., Benneke, B., Deming, D., & Homeier, D. (2014). A featureless transmission spectrum for the neptune-mass exoplanet gj 436b. *Nature*, *505*(7481), 66–68.

Lanzerotti, L., Armstrong, T., Gold, R., Anderson, K., Krimigis, S., Lin, R., ... others (1992). The hot plasma environment at jupiter: Ulysses results. *Science*, *257*(5076), 1518–1524.

Lee, C., Lewis, S. R., & Read, P. L. (2010). A bulk cloud parameterization in a venus general circulation model. *Icarus*, *206*(2), 662–668.

Li, C., Ingersoll, A., Janssen, M., Levin, S., Bolton, S., Adumitroaie, V., ... others (2017). The distribution of ammonia on jupiter from a preliminary inversion of juno microwave radiometer data. *Geophysical Research Letters*, *44*(11), 5317–5325.

Li, L., Jiang, X., West, R., Gierasch, P., Perez-Hoyos, S., Sanchez-Lavega, A., ... others (2018). Less absorbed solar energy and more internal heat for jupiter. *Nature communications*, *9*(1), 1–10.

Lian, Y., & Showman, A. P. (2008). Deep jets on gas-giant planets. *Icarus*, *194*(2), 597–615.

Lian, Y., & Showman, A. P. (2009). Generation of zonal jets by moist convection on the giant planets. *Icarus*.

Lian, Y., & Showman, A. P. (2010). Generation of equatorial jets by large-scale latent heating on the giant planets. *Icarus*, *207*(1), 373–393.

Marley, M. S., & Sengupta, S. (2011). Probing the physical properties of directly imaged gas giant exoplanets through polarization. *Monthly Notices of the Royal Astronomical Society*, *417*(4), 2874–2881.

Moses, J., Fouchet, T., Bézard, B., Gladstone, G., Lellouch, E., & Feuchtgruber, H. (2005). Photochemistry and diffusion in jupiter's stratosphere: constraints from iso observations and comparisons with other giant planets. *Journal of Geophysical Research: Planets*, *110*(E8).

Newman, C. E., Lee, C., Lian, Y., Richardson, M. I., & Toigo, A. D. (2011). Stratospheric superrotation in the titanwrf model. *Icarus*, *213*(2), 636–654.

Newman, C. E., Richardson, M. I., Lian, Y., & Lee, C. (2016). Simulating titan's methane cycle with the titanwrf general circulation model. *Icarus*, *267*, 106–134.

Niemann, H. B., Atreya, S. K., Carignan, G. R., Donahue, T. M., Haberman, J. A., Harpold, D. N., ... others (1996). The galileo probe mass spectrometer: Composition of jupiter's atmosphere. *Science*, *272*(5263), 846–849.

O'Neill, M. E., Emanuel, K. A., & Flierl, G. R. (2015). Polar vortex formation in giant-planet atmospheres due to moist convection. *Nature Geoscience*, *8*(7), 523–526.

Porco, C. C., West, R. A., McEwen, A., Del Genio, A. D., Ingersoll, A. P., Thomas, P., ... others (2003). Cassini imaging of jupiter's atmosphere, satellites, and rings. *Science*, *299*(5612), 1541–1547.

Ragent, B., Colburn, D. S., Rages, K. A., Knight, T. C., Avrin, P., Orton, G. S., ... Grams, G. W. (1998). The clouds of jupiter: Results of the galileo jupiter mission probe nephelometer experiment. *Journal of Geophysical Research: Planets*, *103*(E10), 22891–22909.

Richardson, M. I., Toigo, A. D., & Newman, C. E. (2007). Planetwrf: A general purpose, local to global numerical model for planetary atmospheric and climate dynamics. *Journal of Geophysical Research: Planets*, *112*(E9).

Robinson, T. D., & Catling, D. C. (2012). An analytic radiative-convective model for planetary atmospheres. *The Astrophysical Journal*, *757*(1), 104.

Sagan, C., & Salpeter, E. E. (1976). Particles, environments, and possible ecologies in the jovian atmosphere. *The Astrophysical Journal Supplement Series*, *32*, 737–755.

Seiff, A., Kirk, D. B., Knight, T. C., Mihalov, J. D., Blanchard, R. C., Young, R. E., ... others (1996). Structure of the atmosphere of jupiter: Galileo probe measurements. *Science*, *272*(5263), 844–845.

Senel, C. B., Temel, O., Lee, C., Newman, C. E., Mischna, M. A., Muñoz-Esparza, D., ... Karatekin, O. (2021). Inter-annual, seasonal and regional variations in the martian convective boundary layer derived from gcm simulations with a semi-interactive dust transport model. *Journal of Geophysical Research: Planets*, e2021JE006965.

Showman, A. P., Cho, J. Y., & Menou, K. (2010). Atmospheric circulation of exoplanets. *Exoplanets*, *526*, 471–516.

Skamarock, W. C., Klemp, J. B., Dudhia, J., Gill, D. O., Barker, D. M., Wang, W., & Powers, J. G. (2008). A description of the advanced research wrf version 3. ncar technical note-475+ str.

Smoluchowski, R. (1967). Internal structure and energy emission of jupiter. *Nature*, *215*(5102), 691–695.

Temel, O., Karatekin, Ö., Mischna, M. A., Senel, C. B., Martínez, G., Gloesener, E., & Van Hoolst, T. (2021). Strong seasonal and regional variations in the evaporation rate of liquid water on mars. *Journal of Geophysical Research: Planets*, *126*(10),

e2021JE006867.
Toigo, A. D., French, R. G., Gierasch, P. J., Guzewich, S. D., Zhu, X., & Richardson, M. I. (2015). General circulation models of the dynamics of pluto's volatile transport on the eve of the new horizons encounter. *Icarus*, *254*, 306–323.
Tolento, J. P., & Robinson, T. D. (2019). A simple model for radiative and convective fluxes in planetary atmospheres. *Icarus*, *329*, 34–45.
Wittenmyer, R. A., Butler, R. P., Tinney, C., Horner, J., Carter, B., Wright, D., ... O'Toole, S. J. (2016). The anglo-australian planet search xxiv: the frequency of jupiter analogs. *The Astrophysical Journal*, *819*(1), 28.
Yates, J. S., Palmer, P. I., Biller, B., & Cockell, C. S. (2017). Atmospheric habitable zones in y dwarf atmospheres. *The Astrophysical Journal*, *836*(2), 184.
Young, R. M., Read, P. L., & Wang, Y. (2019a). Simulating jupiter's weather layer. part ii: Passive ammonia and water cycles. *Icarus*, *326*, 253–268.
Young, R. M., Read, P. L., & Wang, Y. (2019b). Simulating jupiter's weather layer. part i: Jet spin-up in a dry atmosphere. *Icarus*, *326*, 225–252.

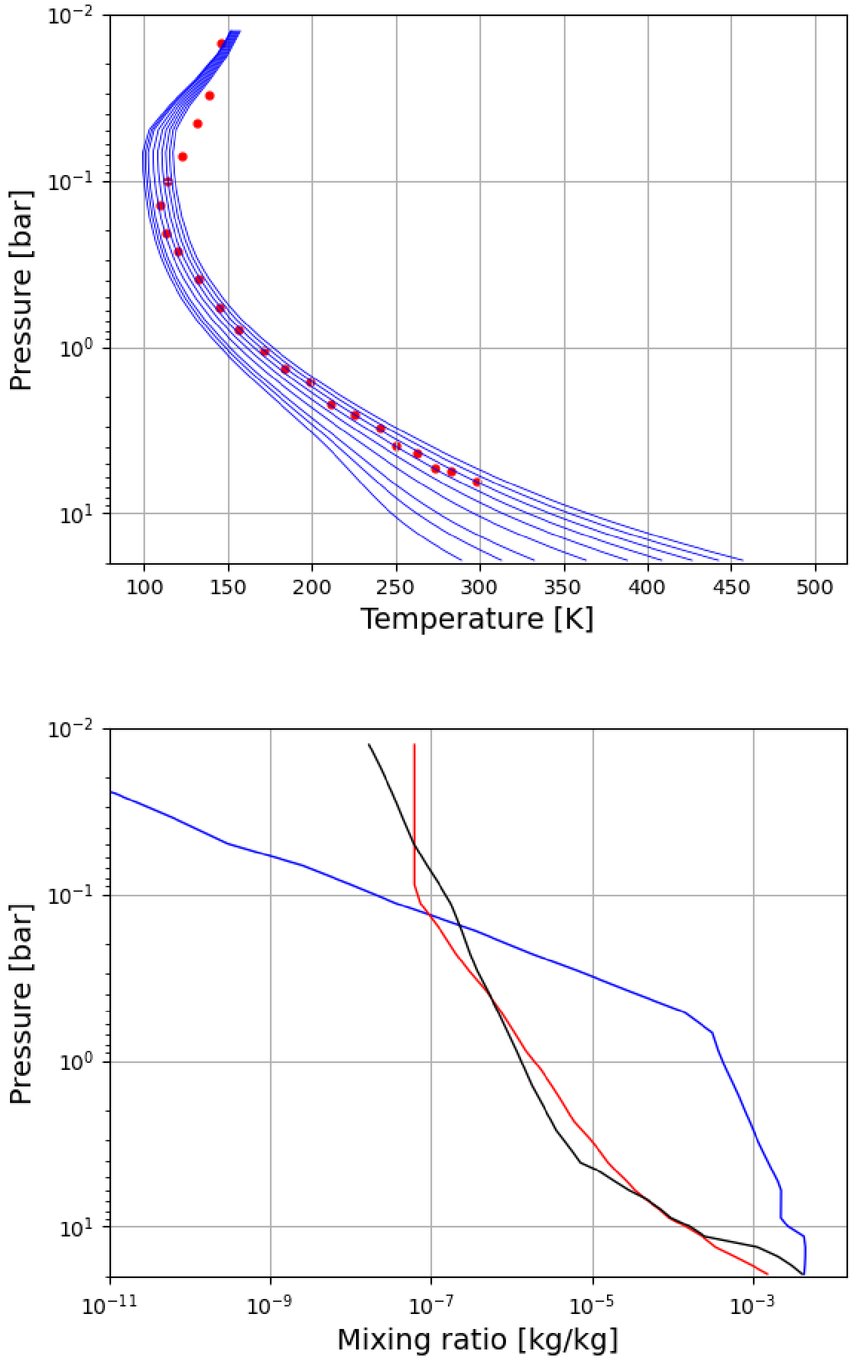

Figure 1. Top panel: (red) Forcing scenarios for different internal heat fluxes, (blue) compared to dataset of (Moses et al., 2005). Red: Nine internal heat fluxes - from left to right: 1.35 W/m^{-2}, 2.025 W/m^{-2}, 2.7 W/m^{-2}, 4.05 W/m^{-2}, 5.4 W/m^{-2}, 6.75 W/m^{-2}, 8.1 W/m^{-2}, 9.45 W/m^{-2}, 10.8 W/m^{-2}. Bottom panel: Initial tracers, blue line - gaseous NH_3, black line - gaseous H_2O, red line - H_2S

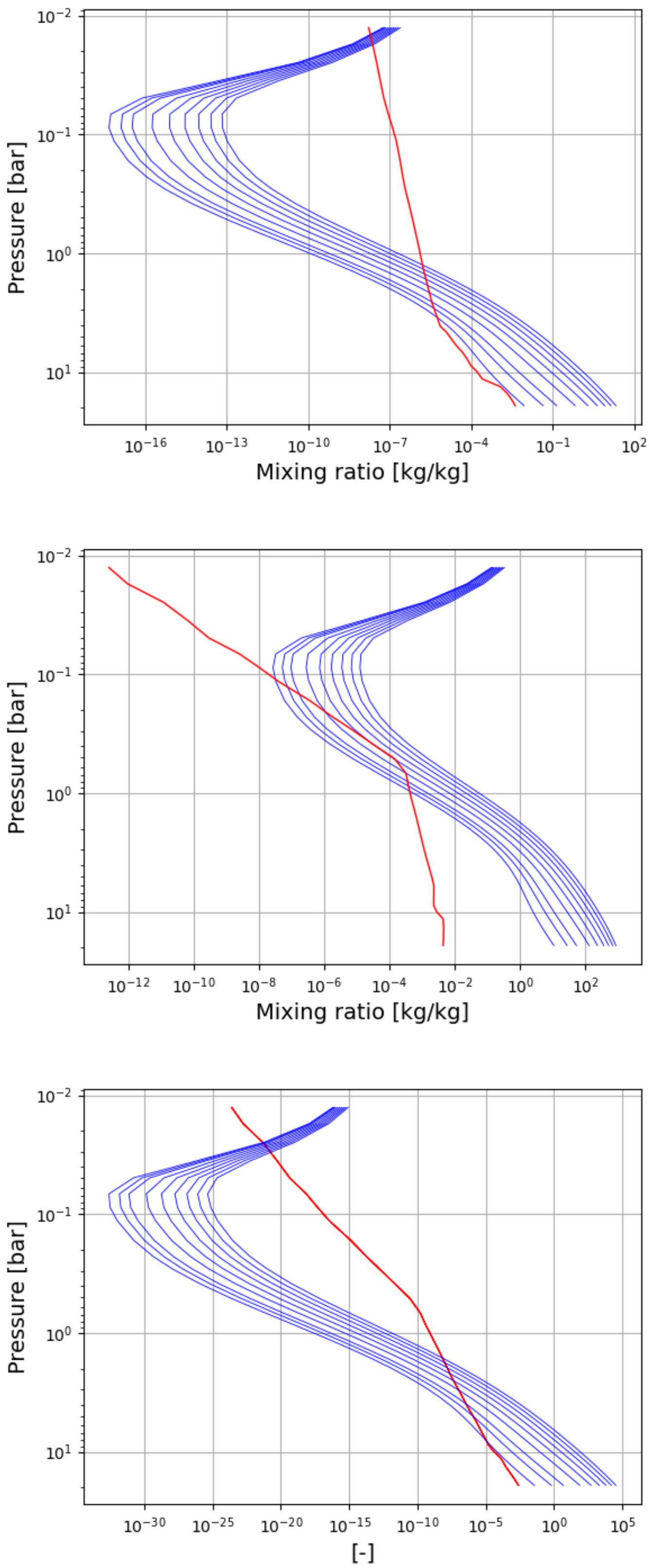

Figure 2. Top panel: Initial distribution of water vapor (blue line) and its saturation mixing ratio of water vapor for nine interior heat fluxes. Middle panel: Initial distribution of gaseous ammonia and its saturation mixing ratio with the same color/line scheme in top panel. Bottom panel: P_{H_2S} [bar] x P_{NH_3} [bar] (red line) vs the empirical reaction limit (exp(34.137 - 10834 K / T [K])) (blue lines). Note that the reaction limit is hence dimensionless (Young et al., 2019a).

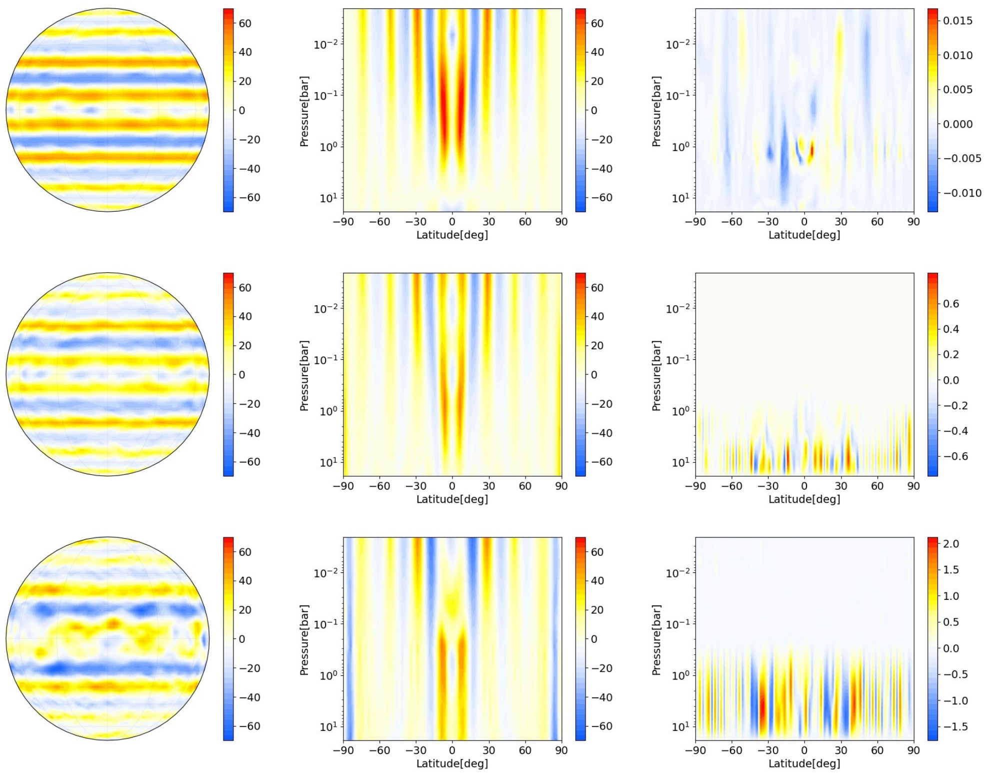

Figure 3. Left column: Zonal winds [m/s] at 0.1 bar for case-L (top), case-M (middle) and case-H (bottom). Middle column : Vertical variation of zonally averaged zonal winds [m/s] for case-L (top), case-M (middle) and case-H (bottom). Right column: Vertical winds [m/s] for case-L (top), case-M (middle) and case-H (bottom).

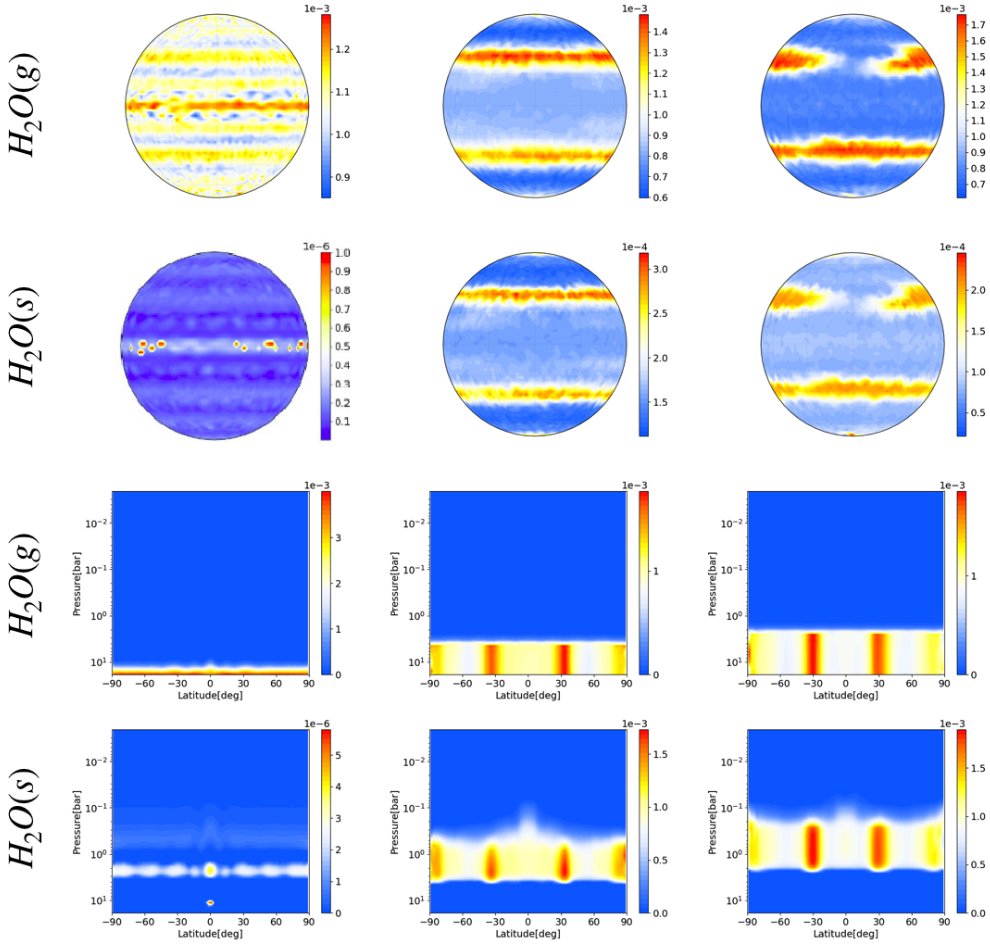

Figure 4. 1st and 2nd panels: Global variation of column integrated water cycle species for interior heat fluxes of F_i = 1.35 W/m^2 (left), 5.40 W/m^2 (middle) and 10.80 W/m^2 (right). 3rd and 4th panels: Vertical variation of zonally averaged water cycle species for interior heat fluxes of F_i = 1.35 W/m^2 (left), 5.40 W/m^2 (middle) and 10.80 W/m^2 (right). Gaseous H_2O: 1st and 3rd panels; solid H_2O: 2nd, and 4th panels.

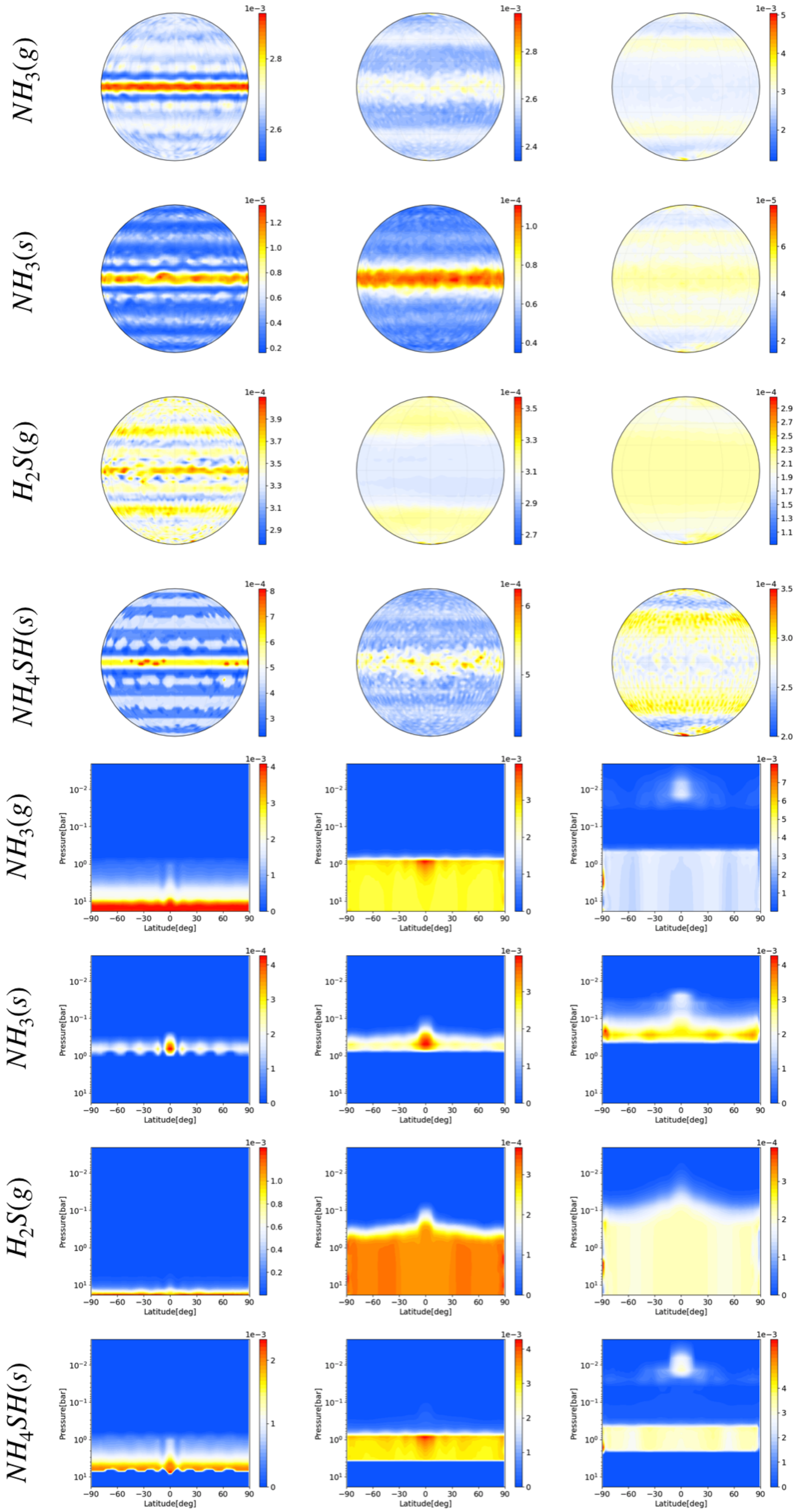

Figure 5. 1st - 4th panels: Global variation of column integrated ammonia cycle species for interior heat fluxes of F_i = 1.35 W/m^2 (left), 5.40 W/m^2 (middle) and 10.80 W/m^2 (right). 5th and 8th panels: Vertical variation of zonally averaged ammonia cycle species for interior heat fluxes of F_i = 1.35 W/m^2 (left), 5.40 W/m^2 (middle) and 10.80 W/m^2 (right). Gaseous NH_3: 1st, 5th panels; solid NH_3: 2nd, 6th panels; gaseous H_2S: 3rd, 7th panels; solid NH_4SH: 4th and 8th panels.

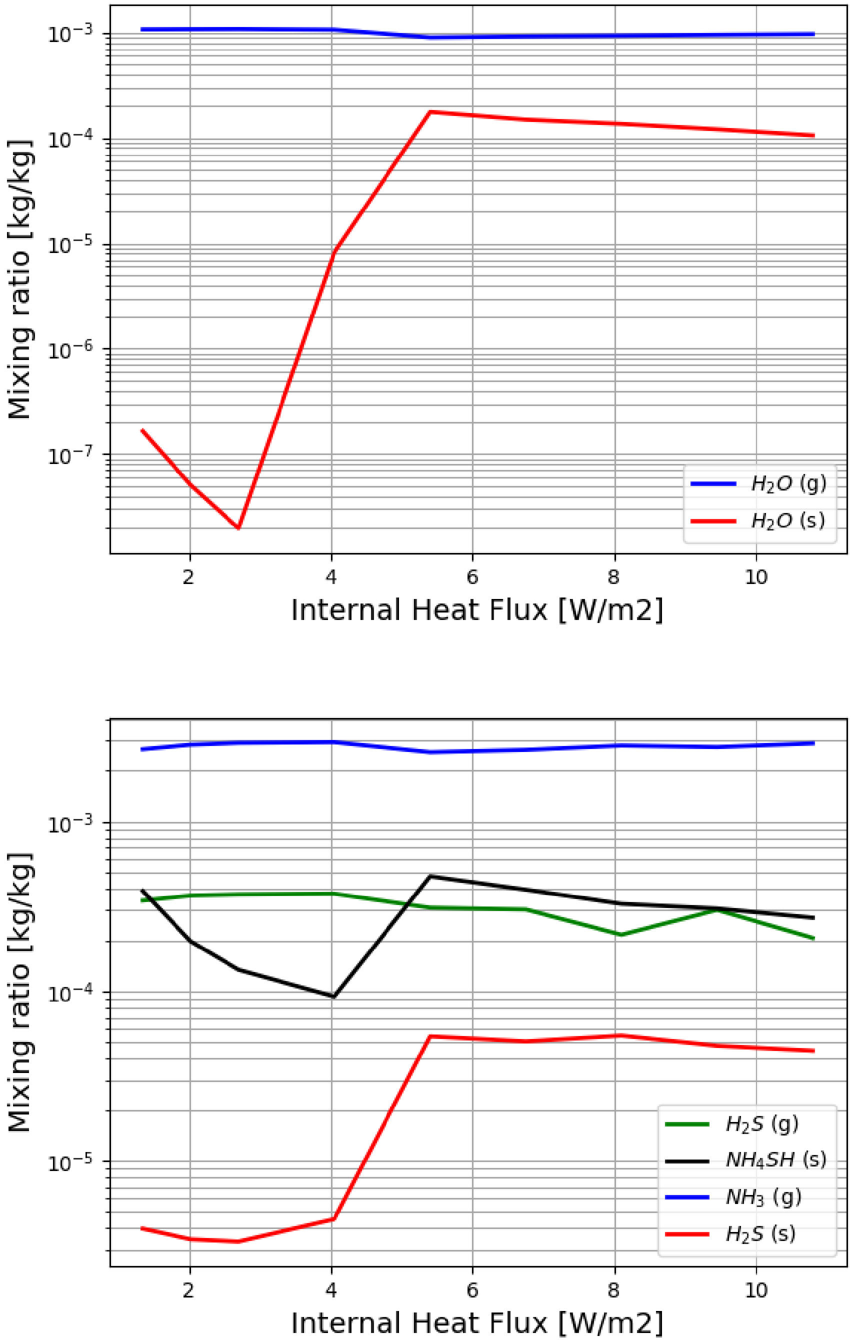

Figure 6. Effect of varying internal heat flux on the globally averaged column integrated water and ammonia cycle species.